TECHNICAL REPORT

Development of hyperspectral camera for auroral imaging (HySCAI)

M. Yoshinuma[1], K. Ida[1*] and Y. Ebihara[2]

Abstract

The hyperspectral camera for auroral imaging (HySCAI), which can provide a two-dimensional (2D) aurora image with full spectrum, was developed to study auroral physics. HySCAI consists of an all-sky lens, monitor camera, galvanometer scanner, grating spectrograph, and electron multiplying charge coupled device (EM-CCD). The galvanometer scanner can scan a slit image of the spectrograph on the all-sky image plane in the direction perpendicular to the slit. HySCAI has two gratings; one is 500 grooves/mm for a wide spectral coverage of 400–800 nm with a spectral resolution (FWHM) of 2.1 nm, and the other is 1500 grooves/mm for a higher spectral resolution of 0.73 nm with a narrower spectral coverage of 123 nm. The absolute sensitivity is 2.1 count/s/R with 4 × 4 binning (256 × 340 image) at 557.7 nm. The exposure time depends on the brightness of the aurora emission and is typically 64 s for a 2D image (0.2 s per line scan). This system has been installed at the KEOPS (Kiruna Esrange Optical Platform Site) of the SSC (Swedish Space Corporation) in Kiruna, Sweden. All-sky images with a liquid crystal filter and a sky color camera have also been installed to compensate for the poor time resolution of HySCAI. 2D aurora monochromatic images for given wavelength are obtained by reconstructing the EM-CCD image over the scan period. HySCAI has the advantage of providing a 2D image of intensity for a weak emission line, which appears on top of a high background emission without the contamination from other emissions, which is usually difficult in a system with a bandpass filter. As the first light results, monochromatic images of N_2^+ 1NG (0, 1) (427.8 nm), N_2^+ 1NG (0, 2) (470.9 nm), H_β (486.1 nm), N II (500.1 nm), N I (^{2}D) (520.0 nm), O I (^{1}S) (557.7 nm,), NaD (589.3 nm), O I (^{1}D) (630.0 nm), and N_2^+ 1NG (670.5 nm) emission intensity were measured. We estimated the precipitating electron energy from a ratio of I(630.0 nm)/I(427.8 nm) to be 1.6 keV.

Keywords Aurora, Hyperspectral camera, Galvanometer mirror, Spectrum, Liquid crystal filter, Precipitating electron energy
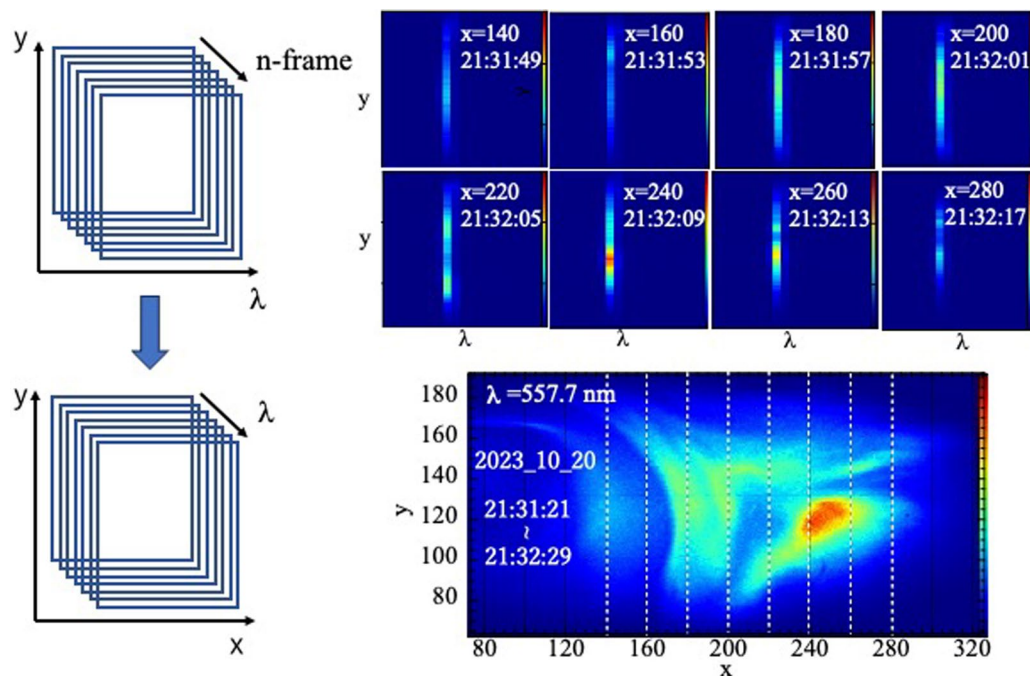
*Correspondence:
K. Ida
ida.katsumi@nifs.ac.jp
Full list of author information is available at the end of the article

Yoshinuma *et al. Earth, Planets and Space*   (2024) 76:96

Page 2 of 16

**Graphical Abstract**

---

1 Introduction

The aurora is a natural luminous phenomenon caused by interactions between precipitating particles and the constituents of the upper atmosphere. Most of the observed spectrum consists of lines or bands of neutral or ionized N_2, O, O_2, and N. The first modern photographic spectrographs were acquired with diffraction gratings by A. B. Meinel in about 1950 (Jones 1974). Comprehensive lists of auroral lines and bands were provided by Chamberlain (1961) and Jones (1971). The wavelength of an aurora is determined by energy levels and transitions of its constituents, as well as vibration and rotational temperatures for molecules and hydrogen lines from protons. Thus, the spectrum of an aurora has a large amount of information about its precipitating particles and atmospheric constituents, as well as mechanisms for auroral emissions. Brekke and Omholt (1968) pointed out that an intensity ratio of I(427.8 nm)/I(557.7 nm) varies by a factor of three in auroral displays. This contradicts the idea that the ratio is almost constant (Rees 1984). Shepherd and Shepherd (1995) suggested that the varied ratio comes from changes in the concentration of atomic oxygen. From an intensity ratio of I(844.6 nm)/I(427.8 nm), Ono (1993) derived the characteristic energy of precipitation electrons in pulsating aurora. He also observed

pulsations at 630.0 nm, and suggested that they were caused by contamination from the N_2 1PG (10, 7) (632.3 nm) band. This implies that spectral observations are needed to reach a definitive conclusion.

A type B aurora (Chamberlain 1961) is one of the most spectacular aurorae, which is characterized by a bright red border at the bottom of the auroral band or curtain. At least, the following five mechanisms have been proposed (Ebihara et al. 2009):

- An increase in the N_2 1PG bands (Vegard and Tønsberg 1936) and an increase in emission from O_2^+ 1NG bands (Dahlstrom and Hunten 1951; Shemansky et al. 1968),
- A decrease in O I (^{1}S) relative to other emissions at the lower auroral border (Evans and Jones 1965; Gattinger and Jones 1979; Jones 1974),
- A shift toward shorter wavelengths in the peak of the N_2 1PG bands (Benesch 1981; Morrill and Benesch 1996),
- An increase in the N_2 1PG bands owing to an accumulation of suprathermal electrons (Hallinan et al. 1997),
- Difference in lifetimes of the N_2 1PG bands and the O I (^{1}S) line (Ebihara et al. 2009; Hallinan et al. 1998; Hanna and Anger 1971).
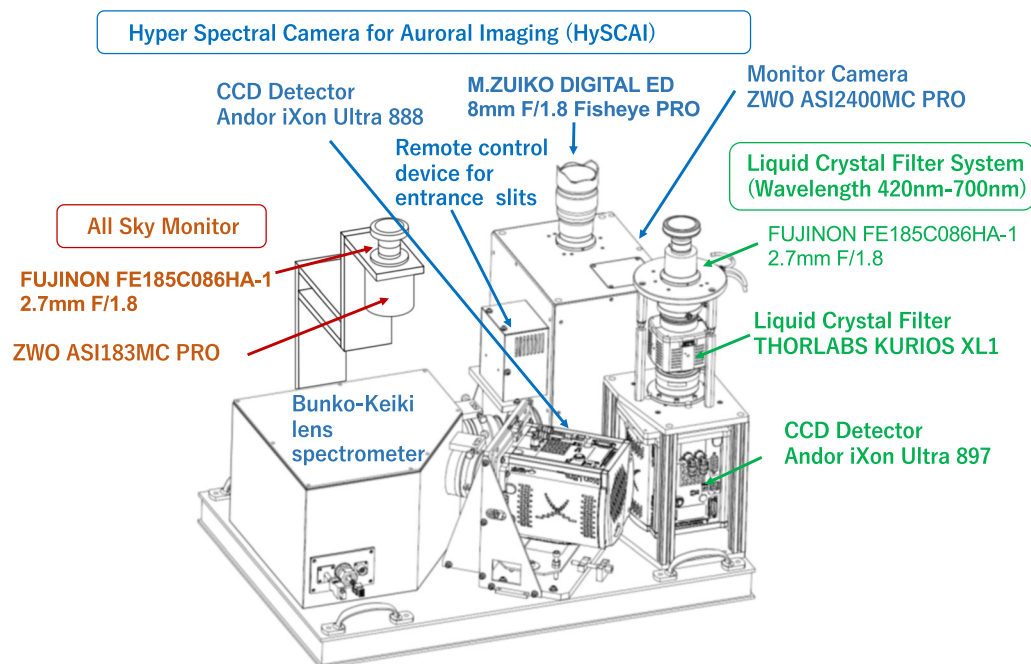
Fig. 1 Schematic view of hyperspectral camera for auroral imaging (HySCAI), all-sky imagers with liquid crystal filter, and all-sky color camera installed at Kiruna, Sweden

Each mechanism listed above is possible, and not exclusive. A question arises as to the relative degree of a visible Type B aurora. Obviously, comprehensive and simultaneous spectrum observations are needed to investigate the Type B aurora.

Spectroscopic measurements of aurorae have been made using interferometric bandpass filters to extract photons in the wavelength range of interest and obtain a two-dimensional image. The multi-spectral camera is widely used as an onboard camera of satellites (Sakanoi et al. 2003; Obuchi et al. 2008; Taguchi et al. 2009) and ground-base all-sky cameras for the observation of aurorae (Stefanello et al. 2015 and STEVE, Yadav et al. 2021). The multi-spectral optical imaging system (MAC) (Sakanoi et al. 2003; Obuchi et al. 2008) using a bandpass filter has been developed for an onboard camera of the Reimei satellite. The MAC system consists of three co-aligned cameras, each with a narrow field of view covering 80 × 80 km at 100 km. Each camera is equipped with a different spectral filter. The telescope of visible light (TVIS) with a filter wheel has also been developed for an onboard camera of the Kaguya spacecraft (Taguchi et al. 2009).

In contrast, a diffraction grating spectrometer has been used to give the full spectrum in ground-based observation of aurorae (Taguchi et al. 2002; Tsuda et al. 2020) and STEVE (Gillies et al. 2019). However, this system gives only one spatial resolution, which is aligned in the meridian direction and does not provide the spectrum of two-dimensional (2D) images. This is because the diffraction grating spectrometer has only spatial resolution along the entrance slit. In order to have spatial resolution perpendicular to the slit direction, a hyperspectral camera for auroral imaging (HySCAI), in which a galvanometer scanner is installed between the image of the all-sky lens and the entrance slit, has been developed. In this paper, the details of the HySCAI design and the results of the first light at the KEOPS (Kiruna Esrange Optical Platform Site) of the SSC (Swedish Space Corporation) in Kiruna, Sweden, are described.

2 Methods

2.1 System layout of hyperspectral camera for auroral imaging (HySCAI)

Figure 1 shows a schematic view of the hyperspectral camera for auroral imaging (HySCAI), all-sky imagers with liquid crystal filter, and a sky color camera installed at Kiruna, Sweden. The hyperspectral camera for auroral imaging (HySCAI), which can provide a two-dimensional (2D) aurora image with full spectrum, was developed to study auroral physics. HySCAI consists of an equisolid angle projection fisheye lens (8 mm F/1.8 M.ZUIKO ED Fisheye PRO), optics for 2D image scan, monitor camera (ZWO ASI2400MC PRO), remote control device for entrance slit, lens spectrometer (Bunko-Keiki), and EM-CCD detector (Andor iXon Ultra 888, 13 μm size 1024

Yoshinuma *et al. Earth, Planets and Space*   (2024) 76:96

Page 4 of 16
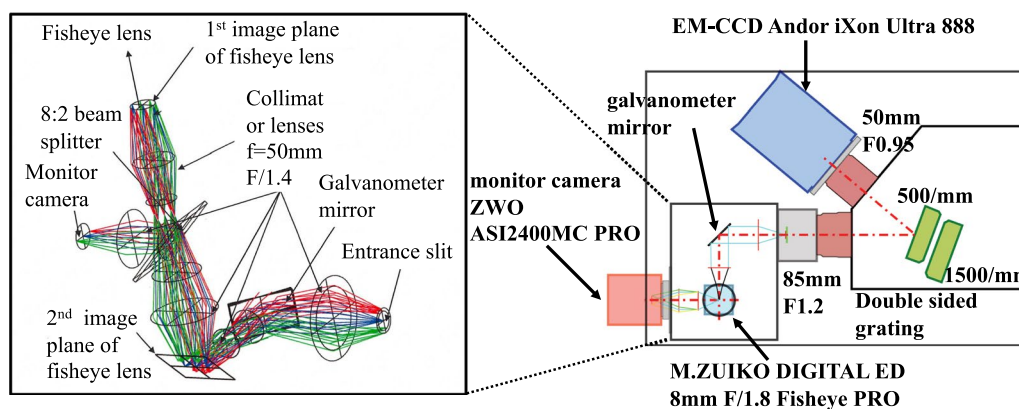
Fig. 2 Optics layout of the control system of hyperspectral camera for auroral imaging (HySCAI)

by1024 pixels, 16 bit resolution). HySCAI has an advantage in providing the 2D image spectrum, but the time for scanning a mirror for a 2D image is relatively long. Therefore, an all-sky color camera and all-sky images with a liquid crystal filter have also been installed to compensate for the poor time resolution of HySCAI. The all-sky color camera consists of an equidistant projection fisheye lens (2.7mm F/1.8 FUJINON FE185C086HA-1) and a digital color camera (ZWO ASI183MC PRO). All-sky images with a liquid crystal filter consist of an equidistant projection fisheye lens (2.7 mm F/1.8 FUJINON FE185C086HA-1), liquid crystal filter (THORLABS KURIOS XL1) coupled with two relay lens, and EM-CCD detector (Andor iXon Ultra 897 16 μm size 512 by 512 pixels). The tunable wavelength of the liquid crystal filter is 420–700 nm.

2.2 Optical layout

Figure 2 shows the optical layout of the hyperspectral camera for auroral imaging (HySCAI). The first image plane of the fisheye lens (8 mm F/1.8 M.ZUIKO ED Fisheye PRO equisolid angle projection) is projected to the entrance slit of the spectrometer using four f = 50 mm F/1.4 collimator lenses. An 8:2 beam splitter is inserted between the first and second image planes of the fisheye lens with the first and second collimator lenses to separate the light of the first image of the fisheye lens to monitor the camera. With this beam splitter, 80% of the light goes to the entrance slit, and 20% of the light goes to the monitor camera (ZWO ASI2400 PRO). A galvanometer mirror is inserted between the second image planes of the fisheye lens and the entrance slit plane with the third and fourth collimator lenses to scan the slit image across the image plane of the fisheye lens. With this scanning galvanometer mirror, a two-dimensional (parallel and perpendicular to the slit direction) image is obtained. The spectrometer comprises two camera lenses (85 mm

F/1.2 and 50 mm F/0.95) and two switchable double-side reflection gratings with groove frequencies of 500/mm and 1500/mm for wide (464 nm) and narrow wavelength range (123 nm) with higher spectrum resolution, respectively, and the EM-CCD camera (Andor iXon Ultra 888). The pixel dispersion is 34.1 nm/mm (0.443 nm/pixel) and 8.232 nm/mm (0.107 nm/pixel) for 500/mm and 1500/mm grating, at 630 nm, respectively. The 500-nm grating can cover the full wavelength from 400 nm to 860 nm, which is necessary for aurora observation. Although this grating can cover O I ($3p^3P$) 844.6 nm, which is one of the candidates for line-ratio measurements, this emission would be blended into the second order of N_2^+ 1NG (0, 1) 427.8 nm, and the sensitivity above 800 nm is too low to measure the intensity of this emission accurately. Here the slit image is reduced by 0.59 using the two camera lenses with focal lengths of 85 mm and 50 mm. To match the F-number of the object lenses (F/1.8), that for the reduced image should be less than 1.06. Therefore, a very low F-number camera lens (F/0.95) is used in front of the EM-CCD detector.

2.3 Control system

As seen in the control system diagram in Fig. 3, a pulse generator (Quantum 9212) sends a frame trigger to the EM-CCD detector and a start trigger to the waveform generator. Since the one frame of the EM-CCD detector consists of spectral data for only one direction parallel to the slit one, several frames are necessary to reconstruct the two-dimensional monochromatic image. The number of frames, n, determines the spatial resolution perpendicular to the slit direction (x direction in this paper). The waveform generator produces a step voltage synchronized with the frame trigger to control the position of the galvanometer, where the angle of the mirror is proportional to the voltage. The step voltage is adjusted to rotate the galvanometer mirror by the slit width (50
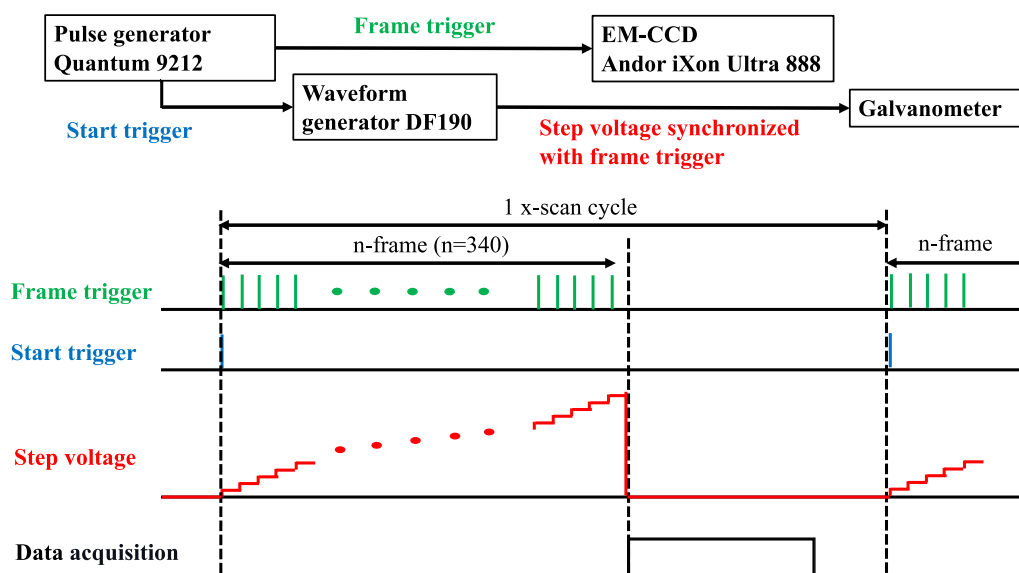
Fig. 3 Schematic diagram of control system of hyperspectral camera for auroral imaging (HySCAI)

μm in standard operation) at the first image plane of the Fisheye lens. To cover the first image plane of the fisheye lens of M.ZUIKO DIGITAL ED 8 mm F/1.8 Fisheye PRO in the x direction (17.2 mm), the number of frame n is set to 340. The data acquired for the n-frame images are written on the hard disk as one file. After creating the file, the next x-scan synchronizes with the next start trigger. The image's time stamp is provided by the Network Time Protocol (NTP) with the PC, which controls the pulse generator Quantum 9212. Depending on the network condition, the accuracy of the time stamp is typically a few milliseconds to a few hundred milliseconds. Therefore, the time stamp using NTP provides the time stamp in the unit of seconds accurately enough.

2.4 Reconstruction of monochromatic image
Figure 4 shows an example of the reconstruction of a monochromatic image from a slit one. The reconstruction of the monochromatic image can be done by simply converting a two-dimensional CCD image of $I(\lambda, y)$ at $t = t_i$ ($i = 1, 2, 3,...$) to a two-dimensional aurora image $I(x, y)$ at $\lambda = \lambda_i$ ($i = 1, 2, 3,...$) using the information of the x-position of each frame. The two-dimensional CCD image of $I(\lambda, y)$ is plotted for $x = 140, 160, 180, 200, 220, 240, 260$, and 280, with 4 s intervals. These eight images show the one-dimensional amplitude profile of a strong emission at $\lambda = 555.7$ nm. Since the exposure time for one frame is 0.2 s and the number of frames is 340, the observation time required for the reconstruction of a monochromatic image is 68 s (21:31:21 UT to 21:32:29 UT on October 20, 2023). By conversion of a two-dimensional CCD image to an aurora one, the monochromatic image at $\lambda = 555.7$ nm is reconstructed, as seen in Fig. 4. It should be noted that the amplitude profile in the y-direction is more accurate than that in the x-direction because the measurements in the former are simultaneous. Because those in the x-direction are sequential, the amplitude profile in that direction is influenced by a change in emission amplitude during the x-scan for a fast-changing aurora, such as a pulsating one. Therefore, a one-dimensional measurement without an x-scan should be done for fast-changing aurorae.

3 Results and discussion
3.1 Spectrum resolution
Spectral resolution was tested with a mercury lamp (Hg lamp) and an He–Ne laser for the liquid crystal filter (LCF) camera and with O I lines (557.7 nm and 630.0 nm) from the aurora emission. The spectrum of the mercury lamp line emission (436 nm, 546 nm, 578 nm) and the He–Ne laser (632.8 nm) were measured by scanning the wavelength of the setting. The spectral resolution and transmission of the LCF camera had strong wavelength dependence. The full width of half maximum measured by the liquid crystal filter camera was 5.9 nm, 9.55 nm, and 11.2 nm at 436 nm, 546 nm, and 632.8 nm, respectively, as seen in Fig. 5a–c. The measured FWHM is very close to the design value of 6.8 nm, 9.6 nm, and 12 nm at 436 nm, 546 nm, and 632.8 nm of Thorlabs KURIOS-XL1. Here the hardware pixel binning of iXon Ultra 888 (13 μ pixel size) was set to 4 × 4 and the binned pixel dispersion was 1.77 nm/bin and 0.428 nm/bin for 500/mm and 1500/mm grating at 630 nm, respectively. The switching time of the liquid crystal filter was < 70 ms, which was

Yoshinuma *et al. Earth, Planets and Space*   (2024) 76:96

Page 6 of 16
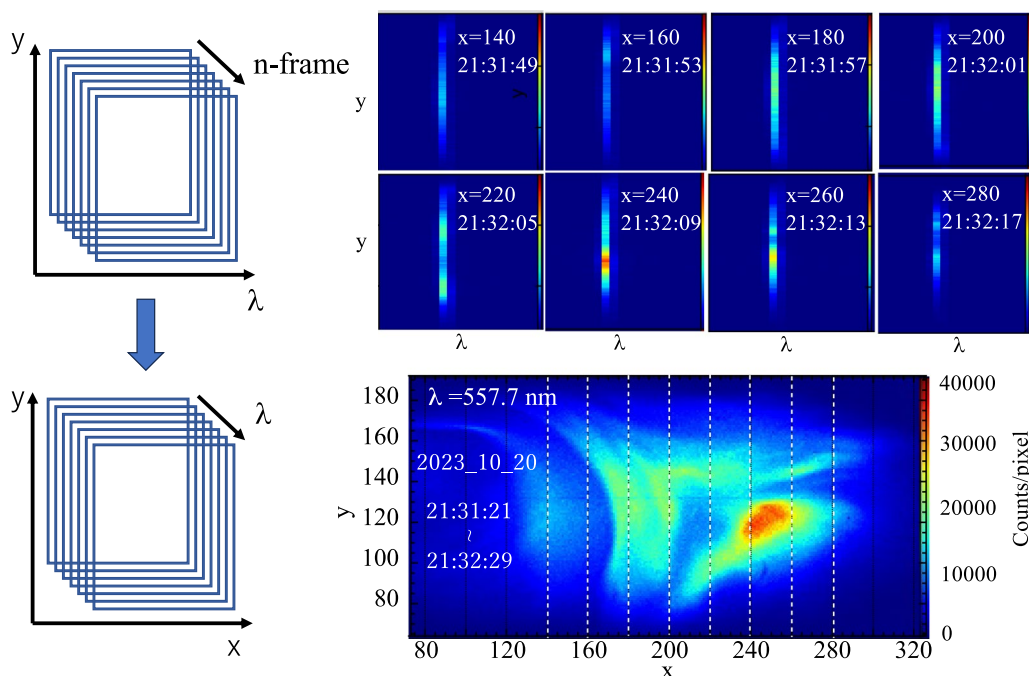
Fig. 4 (top) Original snapshots obtained by HySCAI I(y, λ), and (bottom) reconstructed image (x, y) at 557.7 nm
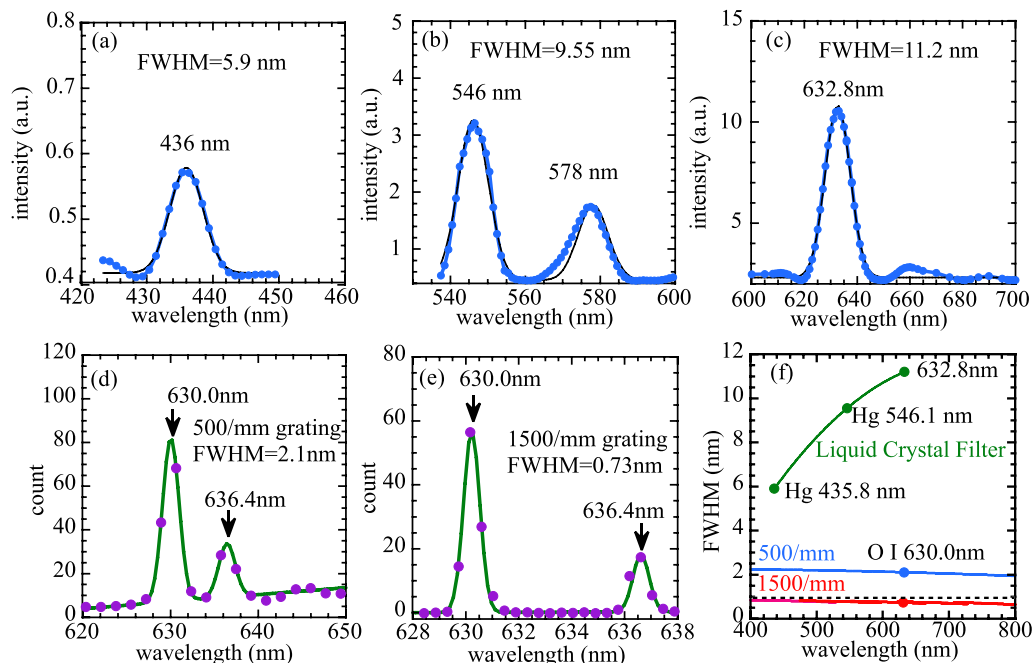
Fig. 5 Spectrum of **a**–**c** all-sky liquid crystal filter (LCF) camera and **d**, **e** hyperspectral camera for auroral imaging (HySCAI) and **f** full width of half maximum (FWHM) of spectrum

fast enough for the aurora observation. In contrast, the spectral resolution of HySCAI was much better than that of the liquid crystal filter. The full width of half maximum measured HySCAI at 630nm was 2.1 nm for the 500/mm

grating and 0.73 nm for the 1500/mm one, for the slit width of (50 μ), as seen in Fig. 5d, e. Because the spectral resolution (FWHM) was roughly proportional to the slit width, one could improve the spectral resolution by
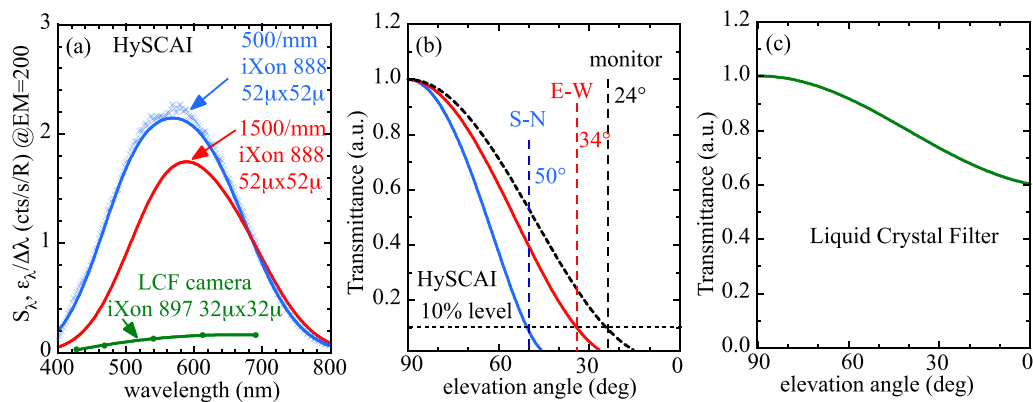
Fig. 6 **a** Wavelength dependence of sensitivity of LCF camera and HySCAI and the relative transmittance of **b** HySCAI and **c** LCF cameras as function of elevation angle in south–north and east–west directions

arrowing the slit. However, the amount of light collected was also proportional to slit width; the spectral and time resolution was a trade-off.

3.2 Sensitivity calibration

Figure 6a shows the wavelength dependence of the sensitivity of the LCF camera and HySCAI, using an integrating sphere and standard lamp (Labsphere HELIOS Plus-VM at the luminance = 18.35×10^3 Cd/m^2, see the REPORT NUMBER: 114672-1-1 for calibrated spectral radiance). The blaze wavelength of the grating is 560nm and 600nm for 500/mm and 1500/mm ones, respectively. The sensitivity of HySCAI has a maximum at the blaze wavelength. Here the hardware pixel binning of iXon Ultra 888 (13μ pixel size) is set to 4×4, and the EM gain at 200. Then the resolution of the binned pixel becomes 256×340. The wavelength dispersion per binned pixel, $\Delta\lambda$, becomes is 1.77 nm and 0.428 nm for the 500/mm and the 1500/mm grating at 630 nm, respectively. The absolute value of the sensitivity is 2.14 and 1.64 counts/second/Rayleigh (c/s/R) at the wavelength of 557.7 nm. In contrast, the sensitivity of the liquid crystal filter camera increases as the wavelength is increased. This is due to the wavelength dependence of polarized transmission (2%, 8%, 18%, 26%, and 39% at wavelengths of 427 nm, 468 nm, 540 nm, 612 nm, and 690.0 nm, respectively). Here the hardware pixel binning of iXon Ultra 897 (16μ pixel size) is set to 2×2, and the EM gain is set at 200. Then the resolution of the binned pixel becomes 256×256. The absolute value of the sensitivity of the LCF camera is 0.14 c/s/R at the wavelength of 557.7 nm. The difference in absolute sensitivity between the HySCAI and LCF cameras is due to the difference in binned sensor size (52 $\mu \times 52\,\mu$ for HySCAI and 32 $\mu \times 32\,\mu$ for LCF camera), the equivalent F-number at the detector (F/1.06 for HySCAI and F/1.8 for LCF camera), and the transmission

at the grating and the filter (65% for HySCAI and 19% for LCF camera).

Figure 6b, c shows the relative transmittance of (b) HySCAI and (c) LCF cameras as a function of the elevation angle in the south–north and east–west directions. This relative transmittance is used to correct the peripheral dimming of the HySCAI and LCF camera systems. The transmittance is evaluated from the ratio of the total intensity (wavelength integrated) of a dawn sky measured by HySCAI and 557.7 nm light measured by the LCF camera to the total intensity (sum of red, green, and blue) measured by the all-sky camera. Even on the monitor camera, there is a significant decrease in transmittance at lower elevation angles. This is due to the peripheral dimming of the light from 1st image plane. The distinct difference between the profile of the monitor camera and that of the E–W of the spectrometer is a direct consequence of the peripheral dimming of the light from the 2nd image plane. Additional peripheral dimming due to the lens inside the spectrometer is seen in the difference between the profiles of E–W and S–N. The attenuation of light intensity of an aurora, due to the absorption and scattering by the atmosphere, varies depending on the wavelength. This attenuation causes large uncertainty in line-ratio measurements, especially at lower elevation angles, where the path lengthens. For this reason, HySCAI is designed to cover only half the sky with a higher elevation angle, ϕ, and a view with more than 10% transmittance is restricted to $\phi > 34°$ in the east–west direction and $\phi > 50°$ in the south–north direction, while the LCF camera covers all sky. HySCAI's south–north corresponds to the slit direction, and its east–west direction corresponds to the scan direction by galvanometer. The narrower view in the south–north direction is due to the peripheral dimming of the spectrometer, which occurs in the slit direction. The view
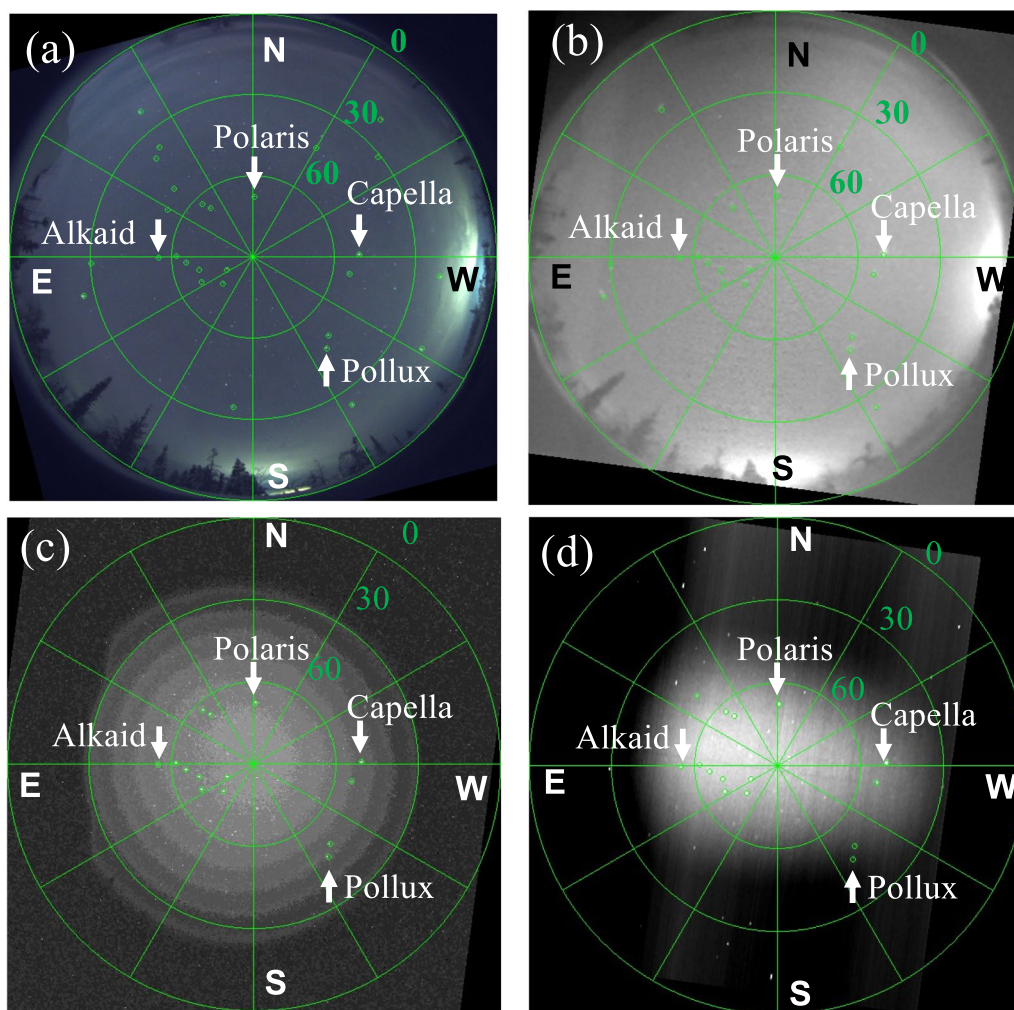
Fig. 7 Examples of spatially calibrated images obtained by **a** all-sky color camera, **b** liquid crystal filter (LCF), **c** HySCAI oriented in S–N vertical direction, and **d** HySCAI oriented in E–W horizontal direction. Small circles indicate star positions at KEOPS (N 67.872° and E 21.030°). Numerical figures, 0, 30, and 60, indicate elevation angles

angle of HySCAI is adjustable (but not remotely.) It can be expanded by replacing the front fisheye lens with a smaller image circle.

3.3 Calibration of elevation angle and azimuth

Space (elevation and azimuth angles) calibration was done by using a position of stars at KEOPS (geographic latitude/longitude N67.872°/E21.030°, geomagnetic latitude N65.37°, and elevation 473 m). The elevation and azimuth angles of the stars were checked using the Stellarium planetarium (Zotti and Wolf 2022; Zotti et al. 2021). Figure 7 shows the images of an all-sky color camera, liquid crystal filter (LCF) camera, and HySCAI oriented in S–N vertical and E–W horizontal directions, where small circles indicate the positions of stars. In the all-sky color camera image, 28 stars were identified (6, 13, and 9 stars at low, medium, and high

elevation angles (0° ∼ 30°, 30° ∼ 60°, and 60° ∼ 90°), respectively) including Polaris, Alkaid, Capella, and Pollux. In contrast, only 18 and 15 stars were identified in the liquid crystal filter camera images and that of HySCAI, respectively. No stars at a low elevation angle (0° ∼ 30°) were identified in the HySCAI image. The start identified with the highest elevation angle was Pollux (47°), which indicated the view of HySCAI as half the all-sky (elevation angle >∼ 45°). The field of view of HySCAI is 0.42° and 0.72°, perpendicular and parallel to the slit direction, respectively

Figure 8 shows an aurora image observed with an all-sky color camera and a monochromatic one at $\lambda = 557.7$ nm, measured by the LCF camera and HySCAI oriented in S–N vertical and E–W horizontal directions, on October 20, 2023. The all-sky color camera images were taken every 12 s and with 5 s exposure time. The
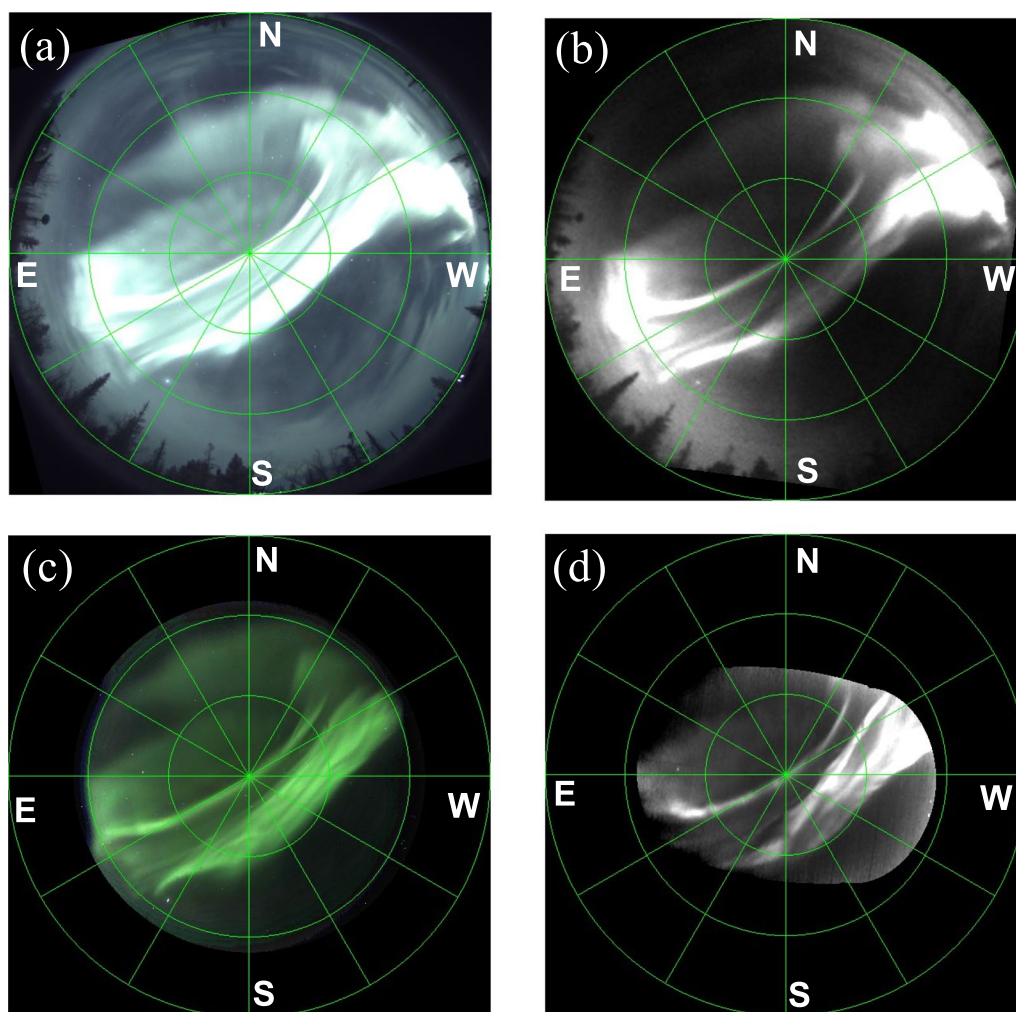
Fig. 8 Calibrated aurora image of **a** all-sky color camera at 21:29:52 ～ 21:29:57 UT, **b** all-sky 557.7 nm imagers with liquid crystal filter at 21:29:53 ～ 21:30:03 UT, **c** HySCAI monitor image at 21:29:49 ～ 21:30:14 UT, and **d** HySCAI reconstructed 557.7 nm image at 21:29:21 ～ 21:30:29 UT on October 20, 2023

LCF camera images were taken every two minutes with 10 s exposure and 7 frames/120 s to check the dynamic change in the 557.7 nm image. HySCAI monitor images were taken every two minutes with 25 s exposures and 2 frames/120 s. A hyperspectral HySCAI image was taken every 2 mins with 68 s (= 0.2 s × 340) exposure time. The HySCAI system could cover only the part of the aurora, due to a restricted view.

3.4 Examples of full spectrum

The spectrum over all positions was averaged to give a quick glance as to which lines appeared in an aurora. Figure 9 is an example of Keogram of all-sky camera and HySCAI, and the time evolution of an averaged spectrum of aurora emission $I_\lambda(\lambda, t)$ measured by HySCAI for ten hours from 2023-10-20 18:00 UT to 2023-10-21 4:00 UT (from 20:24 MLT to 6:24 MLT). The aurora breakups

were seen at 21:30 UT and 23:30 UT in the Keogram of all-sky camera and HySCAI. The view of HySCAI is limited to above 50 degrees of elevation angle. The 400–770 nm wavelength was covered with 500/mm grating. Here the pixel binning of iXon Ultra 888 (13 μ pixel size) was set to 4x4, and the EM gain was set at 200. The data were taken every two minutes. Two strong O I emissions (557.7 nm and 630.0 nm) appeared immediately after the start of the observation at 18:00 UT. The emission amplitude of the spectrum abruptly increased at 21:31:21–21:32:29 UT, which was indicated by white dashed lines on the contour map. The abrupt increase in the emission amplitude was most likely associated with a substorm expansion. The real-time aurora electrojet lowest (AL) index provided by the World Data Center for Geomagnetism in Kyoto showed an abrupt decrease around 21:30 UT. The real-time AL index also showed an abrupt

Yoshinuma *et al. Earth, Planets and Space*   (2024) 76:96

Page 10 of 16
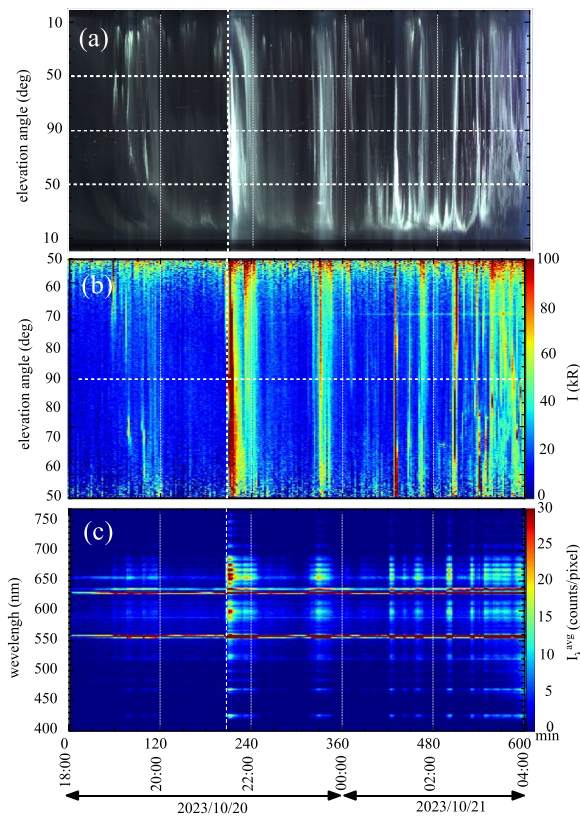
Fig. 9 Keogram of **a** all-sky camera and **b** HySCAI, and **c** time evolution of space-averaged spectrum $I_\lambda^{avg}(\lambda, t)$ of aurora emission measured by HySCAI on October 20–21, 2023

decrease around 23:30 UT, so that the second intensification was associated with the substorm. A strong aurora emission was observed for half an hour.

The space-averaged spectrum $I_\lambda(\lambda)$ is plotted in Fig. 10. Strong oxygen emissions are observed at O I (^{1}S) 557.7 nm, O I (^{1}D) 630.0 nm, and O I (^{1}D) 636.4 nm. The expanded plot in (b) shows several lines of aurora emissions. N_2^+ 1NG (0,1) 427.8 nm and 1NG (0,2) 470.9 nm, N I (^{2}D) 520.0 nm, N_2 1PG (8, 5) 646.9 nm, 1PG (7, 4) 654.5 nm, 1PG (6, 3) 662.4 nm, 1PG (5, 2) 670.5 nm, 1PG (4, 1) 678.9 nm, 1PG (3, 0) 687.6 nm. The ratio between the vibrational levels of N_2 1PG bands can be used to study the effect of collisional processes on N_2 1PG triplet vibrational level populations in aurorae (Morrill and Benesch 1996). O_2^+ 1NG (1,1) 597.3 nm, (0, 0) 602.6 nm, and O II 732/733 nm are also observed. In addition, H_β 486.1 nm and NaD 589.3 nm are also clearly observed. We cannot detect H_α 656.28 nm due to the blend into N_2 1PG. As seen in the spectrum, $\sim$ 20 emissions of atomic and ion lines and molecular bands can be obtained simultaneously. This is a great advantage compared to aurora emission measurements using bandpass filters.

Figure 11 shows the monochromatic image $I_\lambda(\phi, \theta, \lambda_i)$ of N_2^+ 1NG (0,1) (427.8 nm) and O I (^{1}D) (630.0 nm) measured by HySCAI for 40 s from 21:31:37 to 21:32:17 UT on October 20, 2023. It should be noted that HySCAI provides simultaneous measurement in wavelength but not in space, due to the x-scan from east to west by the galvanometer mirror. Here 21:31:37 UT corresponds to the x-scan at 80 (east edge), and 21:32:17 UT T corresponds
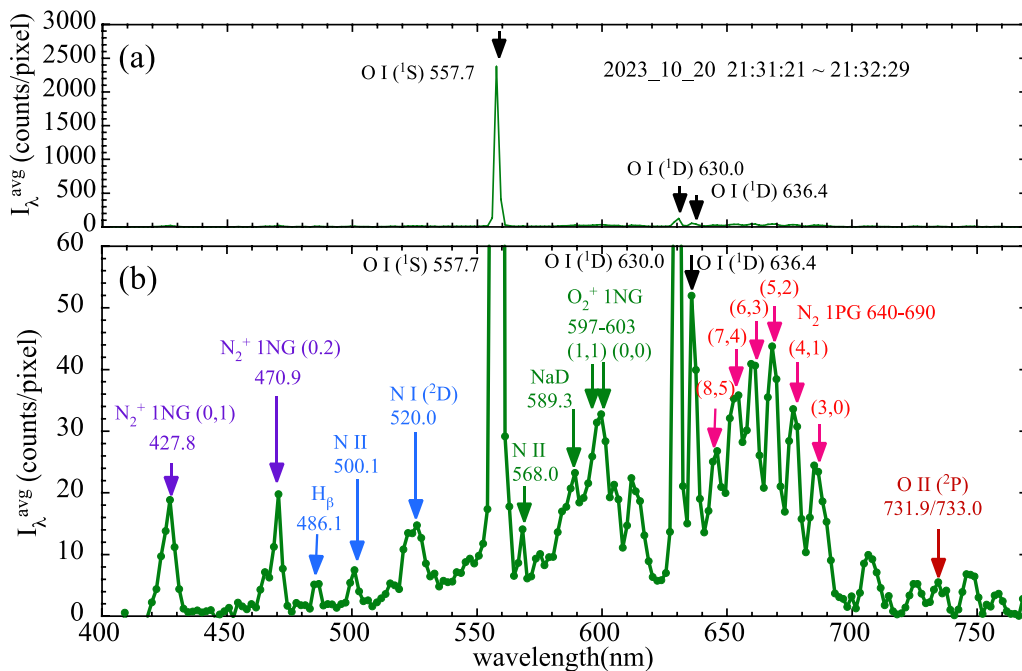
Fig. 10 Space-averaged spectrum $I_\lambda^{avg}(\lambda)$ measured by HySCAI from 21:31:21 UT to 21:32:29 UT (68-s exposure) on October 20, 2023, for the scale of **a** 0–3000 counts/pixel and **b** 0–60 counts/pixel
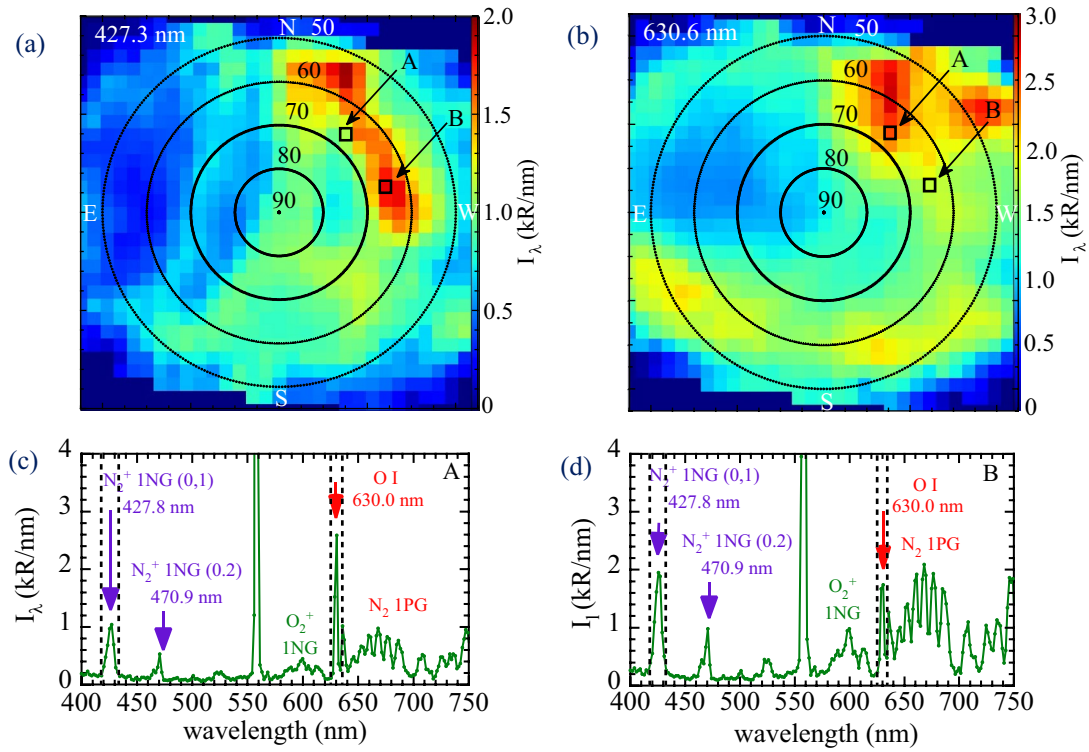
Fig. 11 Monochromatic image $I_\lambda(\lambda_i, \phi, \theta)$ for **a** N_2^+ 1NG (427.8nm) ($\lambda_i = 427.3$ nm) and **b** O I (630.0 nm) ($\lambda_i = 630.6$ nm) and full spectrum $I_\lambda(\lambda, \phi_i, \theta_j)$ at **c** position A ($\phi_i = 67°, \theta_j = 321°$) and at **d** position B ($\phi_i = 64°, \theta_j = 284°$) measured by HySCAI at 21:31:37 ∼ 21:32:17 UT on October 20, 2023

to the x-scan at 280 (west edge). Here, additional 6 x 6 numerical binning is applied to improve the accuracy of the line ratio and the spatial resolution is reduced from 256 × 340 to 42 x 56. The region where the transmittance plotted in Fig. 6 is below 10 % is masked with zero intensity. The two images of O I (^{1}D) (630.0 nm) and N_2^+ 1NG (0, 1) (427.8 nm) show significant differences. The full spectrum $I_\lambda(\lambda)$ at the position A ($\phi_i = 67°, \theta_i = 321°$) and the position B ($\phi_i = 64°, \theta_i = 284°$) is also plotted. Position A ($\phi_i = 67°, \theta_i = 321°$) corresponds to that where the O I (630.0 nm) emission is strong, while position B ($\phi_i = 64°, \theta_i = 284°$) corresponds to the position where the N_2^+ 1NG (427.8 nm) emission is strong. At position A, the emission of both the nitrogen 1NG/1PG and oxygen 1NG bands are relatively strong, while they are much weaker at the position B. The monochromatic image of N_2^+ 1NG (427.8 nm) and O I (630.0 nm) shows that their ratio is not constant in the image.

3.5 Example of monochromatic image of O I, NaD and H$_\beta$

The total intensity of each emission is obtained by integrating the amplitude of the spectrum in wavelength from $\lambda_0 - \delta\lambda_-$ to $\lambda_0 + \delta\lambda_+$, where $\delta\lambda_-$ and $\delta\lambda_+$ are the integration widths at the blue and red sides, respectively,

which is determined from the full spectrum in Fig. 10. Figure 12 shows the monochromatic image $I(\phi, \theta)$ of O I (^{1}S) (557.7 nm, ± 3.3 nm), O I (^{1}D) (630.0 nm, ± 3.2 nm), NaD (589.3 nm, ± 3.2 nm), H$_\beta$ (486.1 nm, ± 3.3 nm), N_2^+ 1NG (0,1) (427.8 nm, −11.3/+4.6 nm), N_2^+ 1NG (0,2) (470.9 nm, −9.2/+3.9 nm), N_2^+ 1NG (5,2) (670.5 nm − 6.6/+1.8 nm), and N I (^{2}D) (520.0 nm, −1.3/+10.7 nm), and N II (500.1 nm, ± 3.3 nm) measured by HySCAI for 40 s from 21:31:37 UT to 21:32:17 UT on October 20, 2023. The region where the transmittance plotted in Fig. 6 is below 10 % is masked with zero intensity. Here the wavelength of the integrated range is indicated as (λ_0, $\delta\lambda_-/\delta\lambda_+$). In calculating a monochromatic image, 4x4 numerical binning is applied to improve the signal-to-noise ratio. The spatial resolution is reduced from 256 × 340 to 64 × 85.

The intensity of most emissions ranges from 1 kR to 10 kR. The emission intensity of N_2^+ 1NG (0,1) (427.8 nm) is 5−15 kR and 8 kR at the geomagnetic zenith (elevation angle (ϕ) of 77.6° and azimuth (θ) of 190.9°). The 427.8 nm emission intensity at the geomagnetic zenith is used to determine the total incident flux, which is one of the input parameters of the code calculating the relation between an intensity ratio of I(630.0nm)/I(427.8nm)
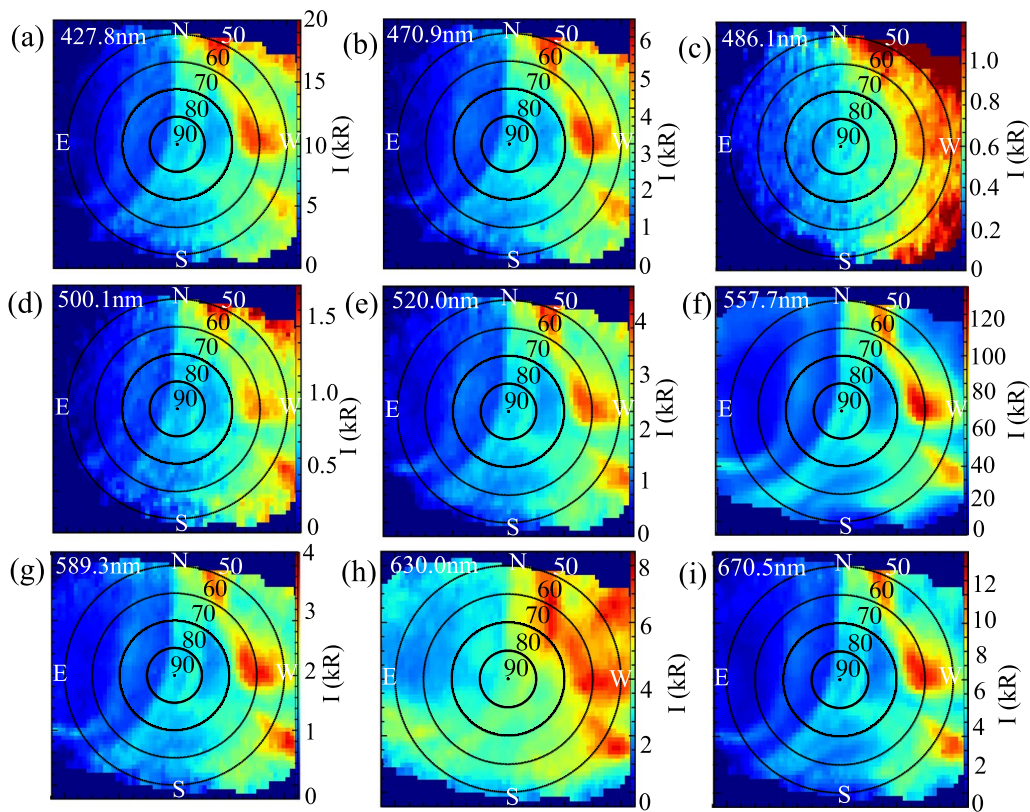
Fig. 12 Monochromatic image $I(\lambda_0)(\phi, \theta)$ of **a** N_2^+ 1NG (0,1) (427.8 nm, −11.3/+4.6 nm), **b** N_2^+ 1NG (0,2) (470.9 nm, −9.2/+3.9 nm), **c** H_β (486.1nm, −2.9/+2.4 nm), **d** N II (500.1 nm, ± 3.3 nm), **e** N I (^{2}D) (520.0 nm, −1.3/+10.7 nm), **f** O I (^{1}S) (557.7 nm, ± 3.3 nm), **g** NaD (589.3 nm, −3.6/+2.3 nm), **h** O I (^{1}D) (630.0 nm, ± 3.2 nm), and **i** N_2^+ 1NG (670.5 nm, −6.6/+1.8 nm) measured by HySCAI at 21:31:37 ~ 21:32:17 UT on October 20, 2023

and the characteristics of energy. The strongest O I (557.7 nm) emission was 40–120 kR, while the weakest H_β (486.1 nm) emission was 0.3–1 kR in this observation. The maximum and noise counts of the iXon Ultra 888 are 65535 and 40, respectively. The saturation level of O I (557.7 nm) emission in this setting (0.2-s exposure and EM gain at 200) evaluated from the sensitivity plotted in Fig. 6(a)(b) is 150 kR at $\phi = 90°$ (250 kR at $\phi = 60°$ and $\theta = 270°$ west). In contrast, the noise level is 0.1 kR. Therefore, the HySCAI has a dynamic range of three orders of magnitude and can simultaneously provide a monochromatic image of strong and weak emissions with a difference of more than two orders of magnitude.

It is clearly observed that the two images of O I (557.7 nm and 630.0 nm) show significant differences, which is due to the difference in height of the aurora emission, where the mean peak emission altitudes of O I (557.7 nm) is ∼ 100 km but the mean peak emission altitude of O I (630.0 nm) is higher (150–350 km) (Whiter et al. 2023). The difference between O I (557.7 nm) and OI (630.0 nm) is mainly due to the difference in lifetime and altitude-dependent constituents and is similar to airglow emissions where the mean peak emission altitude of O I (630.0 nm) is 200–300 km

and is much higher than those of O I (557.7 nm) of 100 km (Shiokawa et al. 1999, 2009). This is because O I (630.0nm) emission becomes weak due to the longer lifetime (110 s lifetime or shorter at lower heights) than the collision time at low altitudes. In contrast, the lifetime of O I (557.7 nm) is 0.7 s, which is shorter than the collision time and can be strong even at low altitude (Tsuda et al. 2020). The image of NaD (589.3nm) resembles the image of O I (557.7 nm). This is because the mean peak emission altitude of sodium line NaD (589.3 nm) is close to that of O I (557.7 nm) because the sodium layer is ∼ 90 km height (Derblom 1964; Shiokawa et al. 1999). Auroral hydrogen emission, H_β, line profiles have been measured to estimate the proton energy of proton aurora (Liang et al. 2018) using a high-resolution spectrometer (Lanchester et al. 2003). Although the emission height for proton auroras is similar to the mean peak emission altitudes of O I (557.7 nm) of ∼ 100 km, the image of H_β differs from that of O I (557.7 nm). The H_β emission profile is much broader than the O I (557.7 nm) one. The diffuse effect in the image is due to the charge exchange between H^+ and neutral constituents (Davidson 1965).
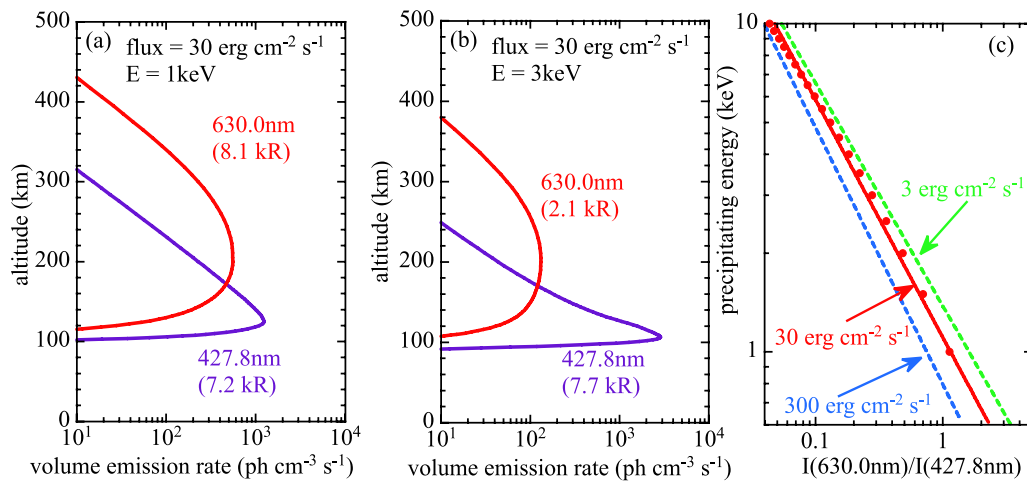
Fig. 13 Volume emission rate vs altitude for the characteristics energy of **a** 1 keV and **b** 3 keV and for the total incident flux of 30 erg cm^{-2} s^{-1}, calculated with GLOW and **c** relation between the characteristic energy and ratio of the integrated volume emission rate of O I (630.0 nm) to that of N$_2^+$ 1NG (427.8 nm) for the total incident flux of 3, 30, and 300 erg cm^{-2} s^{-1}. The values of integrated volume emission along the altitude of O I (630.0nm) to that of N$_2^+$ 1NG (427.8 nm) are also indicated in the unit of kR

3.6 Line ratio of I(630.0 nm)/I(427.8 nm) and estimate of precipitating electron energy

The intensity ratio of auroral emission has been used to estimate the precipitating electron energy (Ono 1993; Whiter et a.l 2012; Grubbs et al. 2017; Redmon et al. 2020; Whiter et al. 2023). A high-speed multi-channel photometer directed to the geomagnetic zenith was developed to estimate the precipitating electron energy (Ono 1993). Auroral lights of different wavelengths were fed into seven channels with beam splitters and dichroic mirrors. The seven emission intensities of N$_2^+$ 1NG (0, 1) 427.8 nm, OI (^{1}S) 557.7 nm, OI (^{1}D) 630.0 nm, N$_2$ 1PG (8, 5) 646.9 nm, N$_2$ 1PG (5, 2) 670.5 nm, O I (3p^{3}P) 844.6 nm were measured simultaneously. It was reported that the individual intense arcs were associated with a significant increase in the precipitating electrons' average energy from 3 to 9 keV during the auroral break-up stage (Reme and Bosqued 1973; Meng et al. 1978; Ono 1993). The 30% change in the average energy of electrons associated with the on/off of pulsating aurorae (Johnstone 1978, Sandahi et al. (1980)) was also reported. More recently, ground-based imaging and in situ sounding rocket data (Sato et al. 2004; Nishiyama et al. 2011) were compared to electron transport modeling for an active inverted-V type auroral event (Grubbs et al. 2017). Electron population characteristics were predicted with a 20% error from the observed spectral intensities within 10° of magnetic zenith.

To evaluate the precipitating electron energy from an intensity ratio of I(630.0 nm)/I(427.8 nm), GLOW 0.973 (Solomon 2017) with Maxwellian energy distribution using an interface of "glowaurora" (https://github.com/

space-physics/glowaurora) and a script of RunGlow. py was used. Figure 13a, b shows the volume emission rate for the characteristics energy of 1 keV and 3 keV at KEOPS (geographic latitude/longitude N67.872°/E21.030°) in 21:31 UT October 20, 2023. Here, the total incident flux is set to 30 erg cm^{-2} s^{-1} where the integrated volume emission of N$_2^+$ 1NG (0,1) (427.8 nm) along the altitude (7.2 kR at 1 keV and 7.7 kR at 3 keV) agrees with that measured (8 kR) at the geomagnetic zenith (elevation angle of 77.6° and azimuth of 190.9°) plotted in Fig. 12a. Here, the value of solar index f10.7 and ap index is set to 124.6 and 6, respectively, which are available at the NASA data center (https://omniweb.gsfc.nasa.gov/form/dx1.html). The mean peak emission altitude of O I (630.0 nm) was 150–250 km, while that of 1NG (0, 1) (427.8 nm) was 100–120 km. The characteristics energy is scanned from 0.5 keV to 10 keV to derive the energy dependence of the intensity ratio of I(630.0 nm)/I(427.8 nm). As the characteristics energy increases, the O I (630.0 nm) volume emission rate decreases, while N$_2^+$ 1NG (427.8nm) volume emission rate increases. Figure 13c shows the relation between the characteristics energy and the ratio of the volume emission rate of O I (630.0 nm) to that of N$_2^+$ 1NG (427.8 nm) integrated along the altitude for the total incident flux of 3, 30, and 300 erg cm^{-2} s^{-1}.

Figure 14a, b shows the image of intensity ratio and precipitating electron energy. The intensity ratio of I(630.0 nm)/I(427.8 nm) varied in space, but it was in the range of 0.4–0.9. The precipitating electron energy was evaluated using the formula of E(keV) = 1.1 × (*I*(630.0n*m*)/*I*(427.8n*m*))$^{-0.72}$ which was derived from
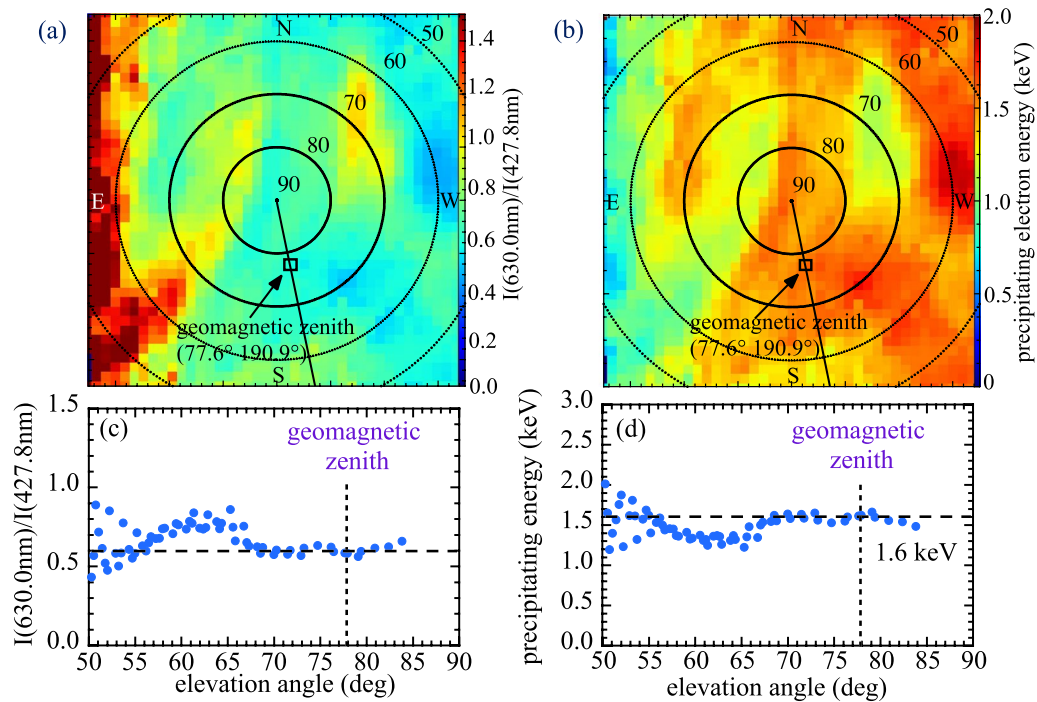
Fig. 14 Image of emission ratio of **a** I(630.0nm)/I(427.8nm) (ϕ, θ) and **b** electron precipitating energy $E(\phi, \theta)$ measured by HySCAI at 21:31:37 ∼ 21:32:17 UT on October 20, 2023. **c** Ratio and **d** electron precipitating energy at azimuth of 191° $\pm$ 5° as function of elevation angle also plotted. Here geomagnetic zenith located at elevation angle of 77.6°, and azimuth of 190.9°

the relation between the intensity ratio of I(630.0nm)/I(427.8nm) and the precipitating electron energy derived from the fitting curve of the data at the total incident flux of 30 erg cm^{-2} s^{-1} plotted in Fig. 13c. Figure 14c, d shows the elevation profile of intensity ratio and precipitating electron energy at azimuth of 191° $\pm$ 5°. We estimated the precipitating electron energy from the ratio of I(630.0 nm)/I(427.8 nm) to be 1.6 keV. The energy had weak dependence for this particular magnetic meridian indicated by the black line. The reason for the weak dependence was that this magnetic meridian indicated by the black line is closely aligned with the auroral structure elongated in the north–south direction, and that the characteristic energy was almost the same along the auroral structure. The line-of-sight integral of the volume emission rates was reasonably accomplished from the bottom to the top of the auroral structure, although the direction of the line of sight was different from that of the magnetic field line.

4 Conclusions

The hyperspectral camera for auroral imaging (HySCAI) was developed to measure the full spectrum of two-dimensional images of aurorae, where a galvanometer mirror scans a slit image. The spectral resolution (FWHM) of HySCAI is 2.1 nm with 500 grooves/

mm grating for a wide spectral range and 0.73 nm with 1500 grooves/mm grating for a higher spectral resolution when the slit width is set to 50 μ. HySCAI can cover a wide wavelength range of 400–800 nm, and the absolute sensitivity is 2.1 count/s/R with 4 × 4 binning (256 × 340 image) at 557.7 nm. The viewing elevation angle > ∼ 45°. The exposure time for one slit image is 0.2 s, and the total scanning time for the two-dimensional image is 68 s. Five oxygen peaks (O I (^{1}S) 557.7nm, O$_2^+$ 1NG (1, 1)(0,0) 597.3/602.6 nm, O I (^{1}D) 630.0nm, O I (^{1}D) 636.4nm O II 732/733), nine nitrogen bands/line (N$_2^+$ 1NG (0, 1) 427.8 nm, 1NG (0, 2) 470.9 nm, N (^{2}D) 520.0 nm, N$_2$ 1PG (8, 5) 646.9 nm, 1PG (7, 4) 654.5 nm, 1PG (6, 3) 662.4 nm, 1PG (5, 2) 670.5 nm, 1PG (4, 1) 678.9 nm, 1PG (3, 0) 687.6 nm) were identified during an aurora substorm on October 20–21, 2023 at KEOPS (Kiruna Esrange Optical Platform Site) of SSC (Swedish Space Corporation) in Kiruna, Sweden. The peak of hydrogen emission H$_\beta$ 486.1 nm and sodium NaD 589.3 nm were also identified. HySCAI provided monochromatic two-dimensional for these peaks. We estimated the total incident flux to be 30 erg cm^{-2} s^{-1} from the emission intensity of N$_2^+$ 1NG (0, 1) 427.8 nm, I(427.8 nm), and the precipitating electron energy to be 1.6 keV from the ratio of I(630.0 nm)/I(427.8 nm) in these observations. The

Yoshinuma *et al. Earth, Planets and Space*   (2024) 76:96

Page 15 of 16

newly developed instrument, HySCAI, will provide new insights into the mechanism of auroral emission as well as the characteristics of precipitating electrons and protons.

Abbreviations

HySCAI	Hyperspectral camera for auroral imaging
LCF	Liquid crystal filter
EM-CCD	Electron multiplying charge coupled device
KEOPS	Kiruna Esrange Optical Platform Site
SSC	Swedish Space Corporation
lc	CCD count per binned pixel
x	Frame numbers of slit image scan (1-340)
y	Binned pixel numbers in the direction parallel to slit (1-256)
$\phi(x,y)$	Elevation angle at the (x,y) position of the original image (zenith: 90°)
$\theta(x,y)$	Azimuth at the (x,y) position of the original image (N: 0° E: 90° S:180° W: 270°)
λ	Wavelength (nm)
R	Rayleigh 10^6 photon/(s cm^2)
$\epsilon_\lambda(\lambda)$	Sensitivity of spectrometer (counts nm/(s R))
$\Delta\lambda(\lambda)$	Wavelength dispersion per binned pixel (nm)
$S_\lambda[=\epsilon_\lambda(\lambda)/\Delta\lambda(\lambda)]$	Sensitivity of camera (counts/s/R)
$T(\phi,\theta)$	Relative transmittance (used for the correction of peripheral dimming)
$I_\lambda(\lambda,\phi,\theta)$	Calibrated spectrum intensity divided by T at $t=t_i$ in the unit of (kR/nm)
$I_\lambda(\lambda_i,\phi,\theta)$	Calibrated spectrum intensity divided by T at $\lambda=\lambda_i$ and $t=t_i$ in the unit of (kR/nm)
$I_\lambda^{avg}(\lambda)$	Space-averaged spectrum intensity at $t=t_i$ in the unit of (counts/pixel)
$I_\lambda^{avg}(\lambda,t)$	Space-averaged spectrum intensity in the unit of (counts/pixel)
$I(\lambda_0)(\phi,\theta)$	Calibrated emission intensity divided by T integrated for $\lambda=\lambda_0\pm\delta\lambda$ in the unit of (kR)
$I(\lambda_1)/I(\lambda_2)(\phi,\theta)$	Ratio of emission intensities of λ_1 to λ_2

Availability of data and materials

The datasets generated and/or analyzed during the current study are available in Data Repository of Aurora Imaging Spectroscopy (DRAIS), https://doi.org/10.57451/nifs.aurora-project.

Declarations

Competing interests

The authors declare that they have no competing of interests.

Author details

[1]National Institute for Fusion Science, National Institutes of Natural Sciences, Toki, Gifu 509-5292, Japan. [2]Research Institute for Sustainable Humanosphere (RISH), Kyoto University, Gokasho, Uji, Kyoto 611-0011, Japan.

References

Benesch W (1981) Mechanism for the auroral red lower border. J Geophys Res 86(A11):9065–9065. https://doi.org/10.1029/JA086iA11p09065

Brekke A, Omholt A (1968) The intensity ratio in aurora. Planet Space Sci 16(10):1259–1264. https://doi.org/10.1016/0032-0633(68)90030-5

Chamberlain JW (1961) Physics of the aurora and airglow. Am Geophys Union. https://doi.org/10.1029/SP041

Dahlstrom CE, Hunten DM (1951) O_2^+ and H in the auroral spectrum. Phys Rev 84(2):378–379. https://doi.org/10.1103/PhysRev.84.378

Davidson GT (1965) Expected spatial distribution of low-energy protons precipitated in the auroral zones. J Geophys Res 70(5):1061–1068. https://doi.org/10.1029/JZ070i005p01061

Derblom H (1964) Observations of sodium emission in aurora. J Atmos Terr Phys 26:791–794. https://doi.org/10.1016/0021-9169(64)90176-X

Ebihara Y, Sakanoi T, Asamura K, Hirahara M, Ieda A (2009) Optical and particle observations of type B red aurora. Geophys Res Lett. https://doi.org/10.1029/2009GL041037

Evans WFJ, Jones AV (1965) Some observations of type-B red aurora with a multichannel photometer. Can J Phys 43(4):697–704. https://doi.org/10.1139/p65-065

Gattinger RL, Jones AV (1979) Observations and interpretation of spectra and rapid time variations of type-B aurora. Planet Space Sci 27(2):169–181. https://doi.org/10.1016/0032-0633(79)90048-5

Gillies DM, Donovan E, Hampton D, Liang J, Connors M, Nishimua Y, Gallardo-Lacourt B, Spanswick E (2019) First observations from the TREx spectrograph: the optical spectrum of STEVE and the picket fence phenomena. Geophys Res Lett 46:7207–7213. https://doi.org/10.1029/2019GL083272

Grubbs G II, Michell R, Samara M, Hampton D, Jahn JM (2017) Predicting electron population characteristics in 2-D using multispectral ground-based imaging. Geophys Res Lett 45:15–20. https://doi.org/10.1002/2017GL075873

Hallinan TJ, Kimball J, Stenbaek-Nielsen HC, Deehr CS (1997) Spectroscopic evidence for suprathermal electrons in enhanced auroras. J Geophys Res Space Phys 102(A4):7501–7508. https://doi.org/10.1029/97ja00197

Hallinan TJ, Kimball J, Osborne D, Deehr CS (1998) Spectra of type-B red lower borders. J Geophys Res 103:11635–11635. https://doi.org/10.1029/97JA03459

Hanna PB, Anger CD (1971) Auroral colour variations. Planet Space Sci 19(4):399–411. https://doi.org/10.1016/0032-0633(71)90046-8

Johnstone AD (1978) Pulsating aurora. Nature 274:119–126. https://doi.org/10.1038/274119a0

Jones AV (1971) Auroral spectroscopy. Space Sci Rev 11(6):776–826. https://doi.org/10.1007/BF00216890

Jones AV (1974) Aurora. Springer, Dordrecht. https://doi.org/10.1007/978-94-010-2099-2

Lanchester BS, Galand M, Robertson SC, Rees MH, Lummerzheim D, Furniss I, Peticolas LM, Frey HU, Baumgardner J, Mendillo M (2003) High resolution measurements and modeling of auroral hydrogen emission line profiles. Ann Geophys 21:1629–1643. https://doi.org/10.5194/angeo-21-1629-2003

Liang J, Donovan E, Gillies D, Spanswick E, Connors M (2018) Proton auroras during the transitional stage of substorm onset. Earth Planets Space 70:126. https://doi.org/10.1186/s40623-018-0899-0

Meng C-I, Snyder AL Jr, Kroehl HW (1978) Observations of auroral westward traveling surges and electron precipitations. J Geophys Res Space Phys 83(A2):575–585. https://doi.org/10.1029/JA083iA02p00575

Morrill JS, Benesch WM (1996) Auroral N_2 emissions and the effect of collisional processes on N_2 triplet state vibrational populations. J Geophys Res 101:261–274. https://doi.org/10.1029/95JA02835

Nishiyama T, Sakanori T, Miyoshi Y, Katoh Y, Asamura K, Okano S, Hirahara M (2011) The source region and its characteristics of pulsating aurora based on the Reimei observations. J Geophys Res Space Phys 116:e2010JA015507. https://doi.org/10.1029/2010JA015507

Obuchi Y, Sakanoi T, Yamazaki A, Ino T, Okano S, Kasaba Y, Hirahara M, Kanai Y, Takeyama N (2008) Initial observations of auroras by the multi-spectral

Yoshinuma *et al. Earth, Planets and Space*   (2024) 76:96

Page 16 of 16

auroral camera on board the Reimei satellite. Earth Planets Space 60:827–835. https://doi.org/10.1186/BF03352834

Ono O (1993) Derivation of energy parameters of precipitating auroral electrons by using the intensity ratios of auroral emissions. J Geomagn Geoelectr 45:455–472. https://doi.org/10.5636/jgg.45.455

Redmon RJ, Denig WF, Kilcommons LM, Knipp DJ (2017) New DMSP database of precipitating auroral electrons and ions. J Geophys Res Space Phys 122:9056–9067. https://doi.org/10.1002/2016JA023339

Rees MH (1984) Excitation of O (^{1}S) and emission of 5577 Å radiation in aurora. Planet Space Sci 32(3):373–378. https://doi.org/10.1016/0032-0633(84)90171-5

Rème H, Bosqued JM (1973) Rocket observations of electron precipitation in a westward-traveling surge. J Geophys Res 7(25):5553–5558. https://doi.org/10.1029/JA078i025p05553

Sakanoi T, Okano S, Obuchi Y, Kobayashi T, Ejir M, Asamura K, Hirahara M (2003) Development of the multi-spectral auroral camera onboard the index satellite. Adv Space Res 32:379–384. https://doi.org/10.1016/S0273-1177(03)90276-6

Sandahl I, Eliasson L, Lundin R (1980) Rocket observation of precipitating electrons over a pulsating aurora. Geophys Res Lett 7(5):309–312. https://doi.org/10.1029/GL007i005p00309

Sato N, Wright DM, Carlson CW, Ebihara Y, Sato M, Saemundsson T, Milan SE, Lester M (2004) Generation region of pulsating aurora obtained simultaneously by the FAST satellite and a Syowa-Iceland conjugate pair of observations. J Geophys Res Space Phys 109:e2004JA010419. https://doi.org/10.1029/2004JA010419

Shemansky DE, Jones AV (1968) Type-B red aurora; the O_2^+ first negative system and the N2 first positive system. Planet Space Sci 16(9):1115–1130. https://doi.org/10.1016/0032-0633(68)90124-4

Shepherd MG, Shepherd GG (1995) On the I(557.7 nm)/I(427.8 nm) emission rate ratio in aurora. J Atmos Terr Phys 57(8):933–943. https://doi.org/10.1016/0021-9169(94)00065-v

Shiokawa K, Katoh Y, Satoh M, Ejiri MK, Ogawa T, Nakamura T, Tsuda T, Wiens RH (1999) Development of optical mesosphere thermosphere imagers (OMTI). Earth Planets Space 51:887–896. https://doi.org/10.1186/BF03353247

Shiokawa K, Otsuka Y, Ogawa T (2009) Propagation characteristics of nighttime mesospheric and thermospheric waves observed by optical mesosphere thermosphere imagers at middle and low latitudes. Earth Planets Space 61:479–491. https://doi.org/10.1186/BF03353165

Solomon SC (2017) Global modeling of thermospheric airglow in the far-ultraviolet. J Geophys Res Space Phys 122:7834–7848. https://doi.org/10.1002/2017JA024314

Stefanello MB, Muella MTAH, Amorim DCM, Machado CS, Bageston JV, Pimenta AA, Martinis C, Sullivan C, Bittencourt JA, Schuch NJ (2015) OI 630.0 nm all-sky image observations of medium-scale traveling ionospheric disturbances at geomagnetic conjugate points. J Atmos Solar-Terr Phys 128:58–69. https://doi.org/10.1016/j.jastp.2015.03.012

Taguchi M, Okano S, Sakanoi T, Koizumi N, Aso T, Ejiri M (2002) A new meridian image spectrograph for the auroral spectroscopy. Adv Polar Upper Atmos Res 16:99–110

Taguchi M, Sakanoi T, Okano S, Kagitani M, Kikuchi M, Ejiri M, Yoshikawa I, Yamazaki A, Murakami G, Yoshioka K, Kameda S, Miyake W, Nakamura M, Shiokawa K (2009) The Upper Atmosphere and Plasma Imager/the Telescope of Visible Light (UPI/TVIS) onboard the Kaguya spacecraft. Earth Planets Space 61:17–23. https://doi.org/10.1186/BF03352980

Tsuda TT, Li C, Hamada S, Hosokawa K, Oyama S-i, Nozawa S, Kawabata T, Mizuno A, Kurihara J, Nishiyama T, Kosch MJ (2020) OI 630.0-nm and N2 1PG emissions in pulsating aurora events observed by an optical spectrograph at Tromsø, Norway. J Geophys Res Space Phys 125:e2020JA028250. https://doi.org/10.1029/2020JA028250

Vegard L, Tønsberg E (1936) Enhancement of red lines and bands in the auroral spectrum from a sunlit atmosphere. Nature 137(3471):778–779. https://doi.org/10.1038/137778b0

Whiter DK, Lanchester BS, Sakanoi T, Asamura K (2012) Estimating high-energy electron fluxes by intercalibrating Reimei optical and particle measurements using an ionospheric model. J Atmos Solar-Terr Phys 89:8–17. https://doi.org/10.1016/j.jastp.2012.06.014

Whiter DK, Partamies N, Gustavsson B, Kauristie K (2023) The altitude of green OI 557.7 nm and blue N2+ 427.8 nm aurora. Ann Geophys 4:1–12. https://doi.org/10.5194/angeo-41-1-2023

Yadav S, Shiokawa K, Otsuka Y, Connors M, St Maurice J-P (2021) Multi-wavelength imaging observations of STEVE at Athabasca, Canada. J Geophys Res Space Phys 126:e2020JA028622. https://doi.org/10.1029/2020JA028622

Zotti G, Wolf A (2022) Stellarium: finally at version 1.0! and beyond. J Skyscape Archaeol 8(2):332–334. https://doi.org/10.1558/jsa.25608

Zotti G, Hoffmann SM, Wolf A, Chéreau F, Chéreau G (2021) The simulated sky: stellarium for cultural astronomy research. J Skyscape Archaeol 6(2):221–258. https://doi.org/10.1558/jsa.17822

Publisher's Note